Pitting corrosion performance for additively manufactured spherical WC/W$_2$C-reinforced stainless steels in chloride-containing solution

Yiqi Zhou[1,2,3),✉], *Peihu Yuan*[1)], *Decheng Kong*[4)], *Xiaochang Xu*[1)], *Shuoyang Wang*[1)], *Lili Li*[1)], *Tingting Liu*[1)], *Xiaogang Li*[1)], *Xuanhui Qu*[1)], *Yu Yan*[1)], *and Chaofang Dong*[1)]

1) Beijing Advanced Innovation Center for Materials Genome Engineering, Institute for Advanced Materials and Technology, University of Science and Technology Beijing, Beijing 100083, China

2) Shunde Innovation School, University of Science and Technology Beijing, Shunde 528399, China

3) State Key Laboratory of Nuclear Power Safety Technology and Equipment, University of Science and Technology Beijing, Beijing 100083, China

4) Shanghai Key Laboratory of Advanced High-temperature Materials and Precision Forming, School of Materials Science and Engineering, Shanghai Jiao Tong University, Shanghai 200240, China

✉Corresponding author: Yiqi Zhou   E-mail: ustbyiqizhou@ustb.edu.cn

Abstract:

One approach to enhance the surface degradation characteristics of laser powder bed fusion (LPBF) type 420 stainless steel involves the incorporation of spherical cast WC/W$_2$C to create LPBF metal matrix composites (MMCs). However, the corrosion behaviour of stainless steel and cast WC/W$_2$C varies inversely with different pH levels, and the phenomenon of pitting corrosion in LPBF MMCs across varying pH conditions has yet to be thoroughly investigated. In LPBF 420 + 5 wt% WC/W$_2$C MMCs, pit occurs adjacent to cast WC/W$_2$C in both acidic and neutral environments, attributed to the presence of chromium-rich carbides and galvanic coupling effects. The dissolution of the reinforced particles facilitates pit nucleation in alkaline conditions. Notably, *in-situ* reaction layers exhibit superior corrosion resistance compared to the matrix or the reinforced particles across all pH levels. The distinct corrosion mechanisms influence the pitting corrosion behaviour, with the corrosion ranking based on critical pitting potential being neutral > alkaline > acidic, which contrasts with the observed kinetics of pit growth (alkaline > acidic > neutral).

1 Introduction:

Type 420 martensitic stainless steel combines high mechanical performance and reasonable corrosion behaviours [1–3]. Laser powder bed fusion (LPBF) technology is one kind of famous additive manufacturing (AM) techniques, which selectively melts the region on the powder bed by high-energy laser in a repeated layer-wise fashion [4–6]. The primary benefits of the LPBF method include the swift fabrication of components without the need for specific designs and the reduction of material waste [5,7]. Type 420 stainless steel is already manufactured by LPBF, which shows excellent mechanical and corrosion resistance [8,9]. There are two approaches to enhance the mechanical characteristics of type 420 stainless steel. The first one is the post-heat treatments; the refining grains and higher carbon in the substrate increase in tensile and hardness properties, and then the change of retained austenite and Cr-rich carbides adjust the mechanical and corrosion performances [10–12]. The second way is by adding reinforced particles, such as TiC, WC, and SiC, to build the LPBF stainless steel-based metal matrix composites (MMCs) [13–16]. In our previous work, the spherical cast WC/W_2C with a size range from $15 - 45$ μm is selected as the reinforced particles, which the lower thermal stability of W_2C releases W and C during laser scanning and react with the matrix to build a solid *in-situ* reaction layer. LPBF $420 + 5$ wt% WC/W_2C MMCs show excellent compressive strength and wear performance [17,18]. The corrosion resistance improved by WO_3 in the passive film and the austenite phase from C in the matrix overcome the degradation from the galvanic coupling between reinforced particles and matrix, resulting in a higher E_{pit} than conventional and LPBF 420 stainless steel [18].

The pitting resistance in the LPBF $420 + 5$ wt% WC/W_2C MMCs is controlled by the most accessible pit nucleation sites in the reinforced particle, *in-situ* reaction

layer, or stainless steel matrix. However, the sensitivity of pitting corrosion in stainless steel and spherical cast WC/W_2C with higher pH values are opposite. The pitting corrosion resistance for stainless steel becomes better with increased pH value in the solution [19,20]. Also, the stability of the passive film in type 304L and type 308L stainless steel increases with higher pH values from 10.5 to 13.5 [21]. However, the changes in corrosion resistance of cast WC/W_2C with increased pH value show the opposite tendency to stainless steel. For example, WC is stable in the acidic and base solution in the WC-Co hard materials, whereas WC becomes less stable in the alkaline environment [22,23]. The stability evolution of the in-situ reaction layer formed between the reinforced particles and the matrix under varying pH conditions remains unclear. Therefore, it is essential to elucidate the pitting corrosion mechanisms for LPBF 420 + 5 wt% WC/W_2C MMCs in acidic, neutral, and alkaline solutions.

The high-throughput research platforms, experimental techniques, and analysis methods, which save time and materials for running experiments, have recently gained attention [24–28]. Bipolar electrochemistry is classified as a high-throughput corrosion testing technique, capable of evaluating the pit nucleation parameters alongside the pit growth rate across a broad spectrum of applied potentials on a single sample following a single test [29–32]. In bipolar electrochemistry, the bipolar electrode (the tested sample) is positioned between the feeder electrodes. Upon the application of a potential or current difference across the feeder electrodes, a linear potential gradient is established. Consequently, the potential difference between the electrolyte and the BPE fluctuates based on the location to the feeder electrode [33–36]. The linear potential gradient observed on the stainless steel BPE leads to varying corrosion responses [37–39]. In the analysis of pitting corrosion, the length of the pit-covered area on the BPE serves as the pit nucleation parameter, while the volume loss due to pit corrosion along the BPE is utilized to derive the kinetics of pit growth [40,41]. In addition to stainless steel, bipolar electrochemistry is employed to investigate the mechanisms of brass dezincification and WC-Co de-alloying [42,43].

This paper aims to study the pitting corrosion resistance of LPBF 420 + 5wt%

WC/W$_2$C MMCs in different pH value solutions. Scanning electron microscopy (SEM) is used to study the microstructure and morphologies of reinforced particles after laser scanning. Transmission electron microscopy (TEM) is chosen to research the *in-situ* reaction layer between the cast WC/W$_2$C and matrix. The passivation in LPBF 420 + 5 wt% WC/W$_2$C MMCs is exalted by potentio-dynamic and potentio-static polarisation tests. The pit initiation and expansion mechanism in H$_2$SO$_4$+ NaCl, Na$_2$SO$_4$ + NaCl, and NaOH + NaCl are studied by bipolar electrochemistry. At last, SEM and laser confocal microscopy investigate the pit corrosion on the BPE tested from different pH solutions.

2 Materials and methods

2.1 Materials

The chemical composition (wt%) of type 420 stainless steel powder is 13.99 Cr, 0.2 C, 0.35 Mn, 0.59 Si, 0.03 Ni, 0.01 Mo, 0.01 P, 0.025 N, and bal. Fe. The type 420 stainless steel and spherical cast WC/W$_2$C powders have the same diameter range between 15 and 45 μm. Both stainless steel and spherical cast WC/W$_2$C powder were produced by Zigong Tungsten Carbide Co. Ltd. Before the LPBF manufacturing, spherical cast WC/W$_2$C and type 420 stainless steel with a weight ratio of 5:95 was mixed by tube roller to prepare the LPBF MMCs raw powder. The LPBF manufacturing environments were 200 °C at the powder bed. An argon gas environment (O < 0.05%) was utilized in the SLM 125HL facility, employing a layer thickness of 30 μm, a hatch spacing of 60 μm, and a 67° rotation between successive printing layers. The scanning speed was set at 950 mm/s, with a laser power of 275 W. All samples analyzed were extracted from planes that are perpendicular to the build direction in LPBF 420 + 5 wt% WC/W$_2$C MMCs, achieving a densification level of 99.82%, as determined by Archimedes' principle.

2.2 Microstructural characterization

The samples with a size of 10 mm x 10 mm x 1 mm (length x width x thickness) were ground at 1200 grits and polished until 1 μm for the microstructure analysis, which was tested by SEM (ZEISS SUPRA55 SEM). To examine the *in-situ* reaction layer between the cast WC/W_2C and the stainless steel matrix, thin lamellae were fabricated from the reinforced particle and the stainless steel matrix utilizing a focused ion beam (FIB, Thermofisher Heilos 5 UX). Subsequently, the microstructure and elemental compositions were analyzed using TEM (FEI G2 F200) integrated with an energy-dispersive X-ray spectroscopy (EDS) system.

2.3 Corrosion tests

0.1M H_2SO_4+ 0.1M NaCl, 0.1M Na_2SO_4 + 0.1M NaCl, and 0.1M NaOH + 0.1M NaCl were selected as acidic, neutral, and alkaline solutions for electrochemistry tests. Before the corrosion test, the surface of the tested samples was checked by optical microscopy to confirm no visible cracks/pores which would influence the corrosion results. For potentio-dynamic and potentio-static polarization assessments, the samples were precisely sectioned to dimensions of 10 mm x 10 mm. Subsequently, the rear side of the LPBF 420 + 5 wt% WC/W_2C MMCs was affixed to a copper wire and embedded in Araldite resin. The exposed surface underwent grinding to a 1200 grit finish, followed by polishing with 1 μm diamond paste to achieve optimal surface quality, then 3M PTFE Tape was used to cover the interface of resin and test sample, which retarded the crevice corrosion during the potentio-dynamic polarization tests, with the tested area reduced to 5 mm x 5 mm. A CS2350 Bipotentiostat associated with CS Studio-5 software was employed for the potentio-dynamic and potentio-static polarization tests. Platinum and saturate calomel electrodes (SCE) were used as the counter and reference electrodes. For the potential-dynamic polarization assessment, the specimen was submerged in the electrolyte for 30 minutes to ensure stabilization of the open circuit potential (OCP). Subsequently, a scan was conducted from 0.2 V below the OCP to 1.0 V vs SCE at a scanning rate of 1 mV/s. In the case of the

potentio-static polarization evaluation, a constant potential of -0.1 V_{SCE}, 0 V_{SCE}, or +0.1 V_{SCE} was applied to the LPBF 420 + 5 wt% WC/W_2C MMCs for a duration of 30 minutes.

Figure 1 gives the schematic diagram of bipolar electrochemistry, where the BPE was situated between two feeder electrodes within the solution. A powder source was utilized to ensure a stable potential across the two feeder electrodes during the bipolar electrochemistry experiment. Upon activation of the power supply, a linear potential developed at the interface of the BPE and the solution. The experimental setup was uncomplicated, requiring only a power supply and two feeder electrodes for the bipolar electrochemistry process. Additionally, the BPE functions wirelessly, allowing for the evaluation of the corrosion behaviour of materials that are either challenging or sensitive to electrical connections. For all bipolar electrochemistry experiments, the sample dimensions were standardized to 30 mm x 15 mm x 1 mm (length x width x thickness), with the surface of the BPE meticulously polished to achieve a finish of 1 μm. The exposure durations for the bipolar electrochemistry were established at 1, 5, and 10 minutes, employing feeder electrodes with a surface area of 4 cm² positioned 50 mm apart. The BPE under investigation was centrally located between the feeder electrodes. A UTP1003S DC power supply was utilized to maintain a constant potential across the two feeder electrodes. After applying 20 V on the feeder electrodes, the anodic electrochemistry reactions occurred next to the negative feeder electrode, and the cathodic electrochemistry reactions nucleated close to the positive feeder electrode. Following the bipolar electrochemistry assessment, SEM was employed to investigate the pitting corrosion mechanism on the LPBF 420 + 5 wt% WC/W_2C MMCs across various pH solutions. Additionally, laser confocal microscopy was selected to analyse the progression of pit formation on the BPEs under differing pH levels and exposure durations.
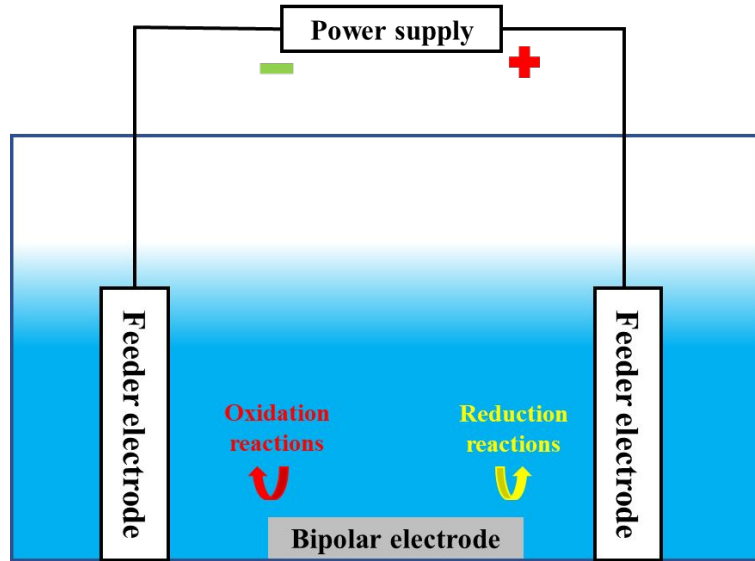
Figure 1 Setup of bipolar electrochemistry.

3 Results and discussion

3.1 Reinforced particles

Figure 2 (a) presents the SEM images of the unprocessed spherical cast WC/W_2C powder, demonstrating that all samples exhibit a high degree of sphericity, free from surface cracks or pores. The superior sphericity of the cast WC/W_2C is expected to maintain the flowability of the LPBF raw powders when blended with 420 stainless steel powder. Figure 2 (b) displays the reinforced particles (relatively white) in the LPBF 420 + 5 wt% WC/W_2C MMCs, which the surface is without cracks or pores obtained at this magnification. The shape of the cast WC/W_2C varies, and the relatively large particles maintain a good circular shape, and the small size particles are irregular. The relationship between the reinforced particles size and geometry can be explained by the Gibbs - Thompson equation [44]:

$$\frac{C_{r1}}{C_{r2}} = exp\left[\frac{3\sigma M}{RT\rho}\left(\frac{1}{r_1} - \frac{1}{r_2}\right)\right] \tag{3}$$

C_{r1} and C_{r2} represent the particles with sizes r_1 and r_2, respectively. The symbol σ denotes the interfacial tension between the reinforced particles and the liquid stainless steel. M refers to the molecular weight of the reinforced particles, R is the universal

gas constant. T indicates the temperature of the molten pool (K), and ρ signifies the density of the cast WC/W$_2$C. So, the larger reinforced particles have minor dissolution during laser scanning, which can maintain a spherical shape; the small size reinforced particles can be dissolved more easily during laser scanning, resulting in the irregular shape of cast WC/W$_2$C. Figure 2 (c) illustrates a cast WC/W$_2$C particle size exceeding 35 μm. The morphology of the reinforced particle retains a spherical form, indicating a low dissolution degree of the strengthen particle, accompanied by a consistent dissolution rate at the interface between the reinforced particles and the matrix. An enhanced magnification of the interface between the reinforced particle and the matrix is presented in Figure 2 (d), a fur-like structure is found between the cast WC/W$_2$C and matrix, which is the *in-situ* reaction layer. So, the *in-situ reaction* layer is built between the strengthened particle and stainless-steel matrix, causing even a tiny dissolution of the spherical. Figure 2 (e, f) illustrates two irregularly shaped cast WC/W$_2$C on the matrix, with a size of 10 μm x 20 μm. The irregular shape comes from different dissolution degrees at the cast WC/W$_2$C. The net-like *in-situ* reaction layer is also found, as shown in Figure 2 (f). The dense crack-pore-free *in-situ* reaction layers next to all the reinforced particles indicate excellent mechanical bonding, which benefits the mechanical and corrosion resistance.
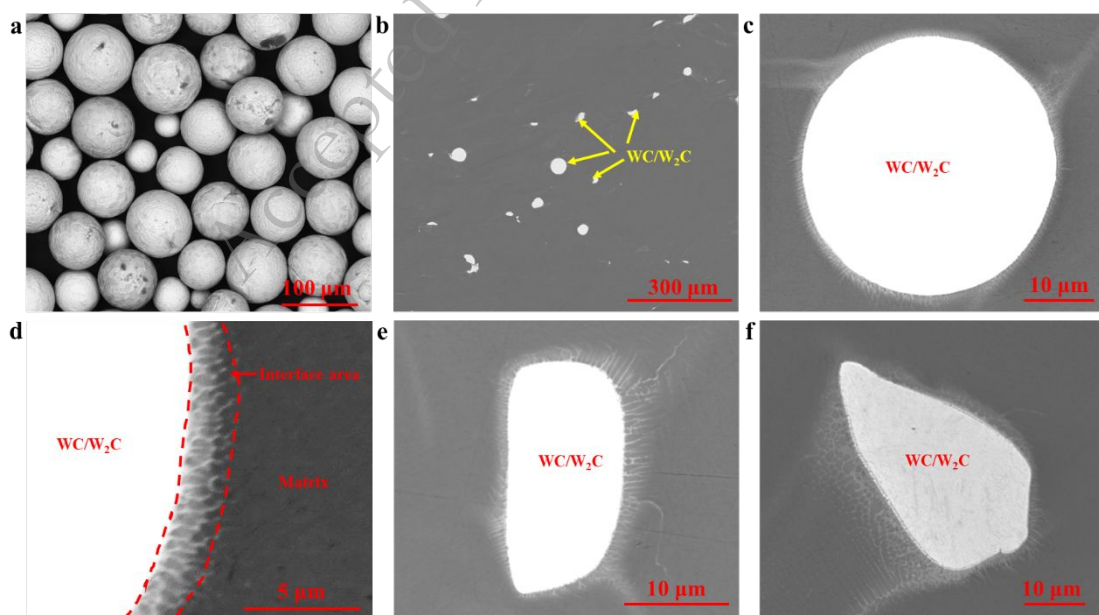

Figure 2 (a) geometry of spherical cast WC/W$_2$C raw powder, (b) shapes of reinforced particles in

LPBF 420 + 5 wt% WC/W$_2$C MMCs, with (c-f) individual reinforced particle at higher magnifications.

3.2 *In-situ* reaction layer

A TEM image includes reinforced particles, an *in-situ* reaction layer, and the matrix is displayed in Figure 3, the same as our previous work [17]. Figure 3 (a) shows four areas labelled I, II, III, and IV. The brightness region is in Region I, which is the cast WC/W$_2$C. Region II contains a dense, bar-like structure towards the stainless-steel matrix, which should be the *in-situ* reaction layer. In Region III, some nano-size precipitates are obtained. The large spherical (up to 50 nm) and small irregular (up to 10 nm) shape precipitates are obtained, as shown at higher magnification in Figure 3 (b). The point edx response in Region II, Region III, and Region IV is displayed in Table 1. In Region II, the weight percentage for Fe, W, and Cr are 18.79 wt%, 35.5 wt%, and 2.2 wt%. The composition of elements in Region III and Region IV is similar, with Fe and W being 17 wt% and 11 wt% lower than in Region II, respectively. Similar elements are detected in Region III and Region IV, indicating both are the matrix of LPBF 420 + 5 wt% WC/W$_2$C MMCs. The precipitates in Region III come from the *in-situ* reaction layer. However, the limited dissolution of the cast WC/W$_2$C and short diffusion time result in precipitates forming at a longer distance to the strengthened particles instead of forming the *in-situ* reaction layer. Figure 3 (c) and Figure 3 (d) give the spherical precipitates with sizes from 50 nm − 70 nm in region III and the matrix far from the reinforced particles, respectively. From the edx response, the precipitates have higher Fe/Cr content and lower W in the stainless steel matrix than in region III, which is related to the longer distance to cast WC/W$_2$C. The Cr in the precipitates is higher than the surrounding matrix, which might form a Cr-depletion region next to the precipitates, sensitive to pitting corrosion [45,46]. Besides the Cr-depletion region, the galvanic effects between the precipitates and matrix also might accelerate the pitting corrosion [47].
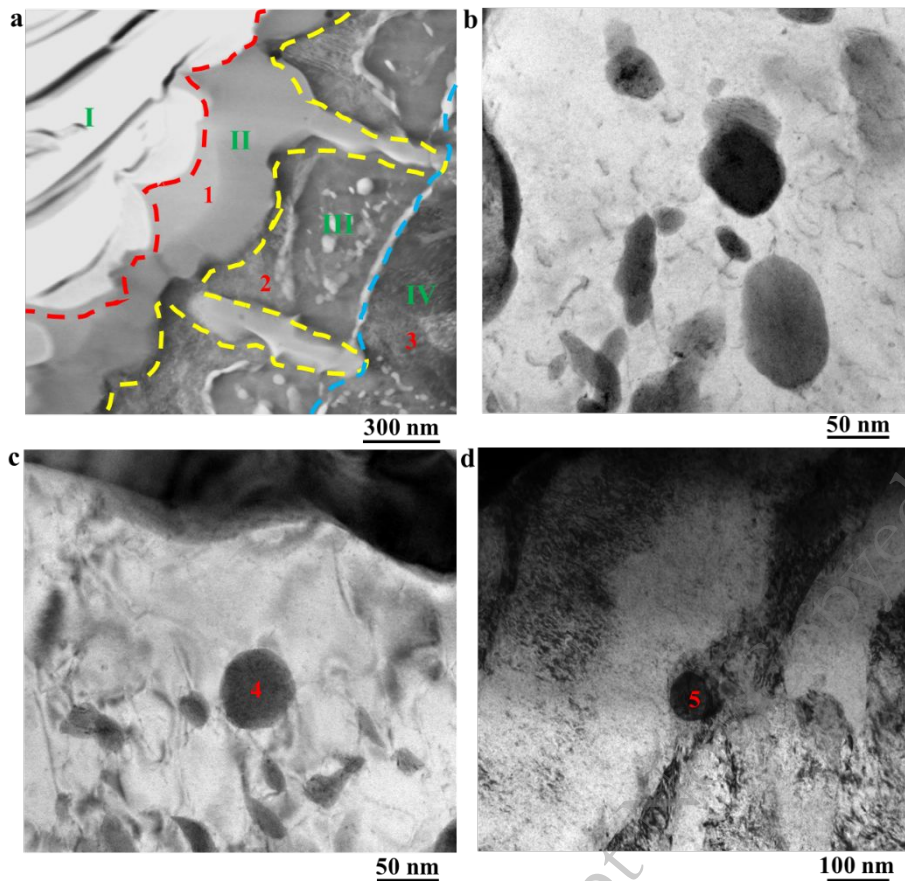
Figure 3 TEM images at (a) interface of cast WC/W$_2$C and matrix, (b,c) high magnification precipitates next to *in-situ* reaction layer, (d) a precipitate in far from the reinforced particle.

Table 1 Element composition at different locations from Fig. 3

Wt%	Fe	W	Cr	C
1	18.79	35.5	2.2	43.51
2	35.71	23.53	2.26	38.50
3	35.04	22.82	2.76	39.38
4	26.55	23.38	6.16	43.91
5	41.16	13.54	8.66	36.64

3.3 Corrosion behaviour

Figure 4 shows the potentio-dynamic polarisation tests for LPBF 420 + 5 wt% WC/W$_2$C MMCs from solutions with varies pH levels. Three independent polarisation tests were done in different pH value solutions to ensure repeatable results, with all potentio-dynamic polarisation curves are displayed. The E_{corr} value for LPBF 420 + 5 wt% WC/W$_2$C MMCs in NaCl + Na$_2$SO$_4$ is around -0.2 V$_{SCE}$,

higher than that ($\approx$ -0.5 V_{SCE}) in H_2SO_4+ NaCl and NaOH + NaCl. In H_2SO_4 + NaCl, the current density rises with an increased in the applied potential up to 0 V_{SCE}, after which it stabilizes at approximately 0.32 mA/cm^2; at last, the current density suddenly increases again at about 0.65 V_{SCE}, indicating the formation of pitting corrosion. For the potentio-dynamic polarisation test, the current density tested in Na_2SO_4 + NaCl is the lowest in all solutions, stabilized at about 0.01 mA/cm^2 from 0.2 V_{SCE} to 1.0 V_{SCE}. After the potentio-dynamic polarisation experiment, no pits were found. However, our previous work found that + 0.38 V_{SCE} is the E_{pit} for LPBF 420 + 5 wt% WC/W_2C MMCs in 0.1M NaCl [18], caused by the competitive adsorption of SO_4^{2-} and Cl^- on the surface, which inhibits the formation of pits [48,49]. Interestingly, the current density obtained in the alkaline solution is higher than the neutral solution. The higher current density in LPBF 420 + 5 wt% WC/W_2C MMCs comes from the dissolution of cast WC/W_2C, which is unstable in the alkaline environment [50,51]. The current density in LPBF 420 + 5 wt% WC/W_2C MMCs diminishes with an increase in potential up to +0.2 V_{SCE}, after which the current density escalates as the applied potential continues to rise. So, +0.2 V_{SCE} should be the critical potential to accelerate the corrosion rate, coming from the faster dissolution of cast WC/W_2C. Faster growth for current density is also found in WC-based hard materials (alloying with Co, Ni, CoCr, and NiCrMo) at about +0.2 V_{SCE} tested in 0.1M NaOH solutions [22,42]. Nevertheless, the potentio-dynamic polarization tests yielded no evidence of pitting, suggesting that the reinforced particle does not initiate pits in LPBF 420 + 5 wt% WC/W_2C MMCs when exposed to 0.1M NaOH + 0.1M NaCl. Additionally, elevated pH levels exacerbate pitting corrosion in stainless steel [52]. Usually, the lower passive current density indicates the higher critical pitting potential in stainless steel. The pitting corrosion rank according the passive current density might be neutral > alkaline > acidic [53].
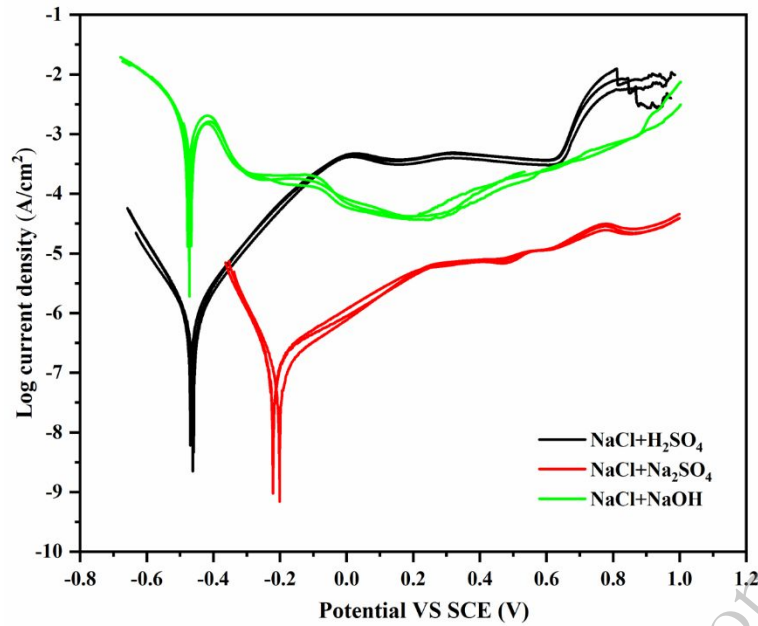
Figure 4 Potentio-dynamic polarisation test of LPBF 420 + 5 wt% WC/W$_2$C MMCs from acidic, neutral, and alkaline solutions.

Figure 5 illustrates the current density response of LPBF 420 + 5 wt% WC/W$_2$C MMCs at a constant potential of -0.1 V$_{SCE}$, 0 V$_{SCE}$, and 0.1 V$_{SCE}$ across various pH solutions. In Figure 5 (a), the potentio-static polarization at -0.1 V$_{SCE}$ for LPBF 420 + 5 wt% WC/W$_2$C MMCs shows a rapid decline in current density for the first 200 seconds, after which it stabilizes with prolonged exposure. The lowest current density response is observed in the Na$_2$SO$_4$ + NaCl solution, followed by H$_2$SO$_4$ + NaCl and NaOH + NaCl. The current density responses at 0 V$_{SCE}$ and 0.1 V$_{SCE}$ are depicted in Figure 5 (b) and (c), respectively. For the NaOH + NaCl solution, the current density decreases over time, whereas the acidic solution exhibits an opposite trend, with a slight increase in current density after reaching a stable value. In neutral solutions, the current density remains relatively constant over time once stability is achieved. Figure 5 (d) summarizes the average current density and standard deviation from 1200 s to 1800 s for both -0.1 V$_{SCE}$ and 0.1 V$_{SCE}$, revealing the highest current density in the NaOH + NaCl solution and the lowest in Na$_2$SO$_4$ + NaCl. A linear correlation between average current density and applied potential is observed across all solutions, with the slope indicating the sensitivity of current density to increasing applied

potential. The steepest slope is recorded in NaOH + NaCl, suggesting that the surface passive film becomes increasingly unstable with higher applied potential. Conversely, the lowest slope in Na_2SO_4 + NaCl indicates that the passive film is more effective in maintaining passivation as the applied potential increases. In acidic environments, the current density is lower than in alkaline conditions, attributed to the formation of corrosion products that cover the sample surface, thereby reducing the corrosion rate.
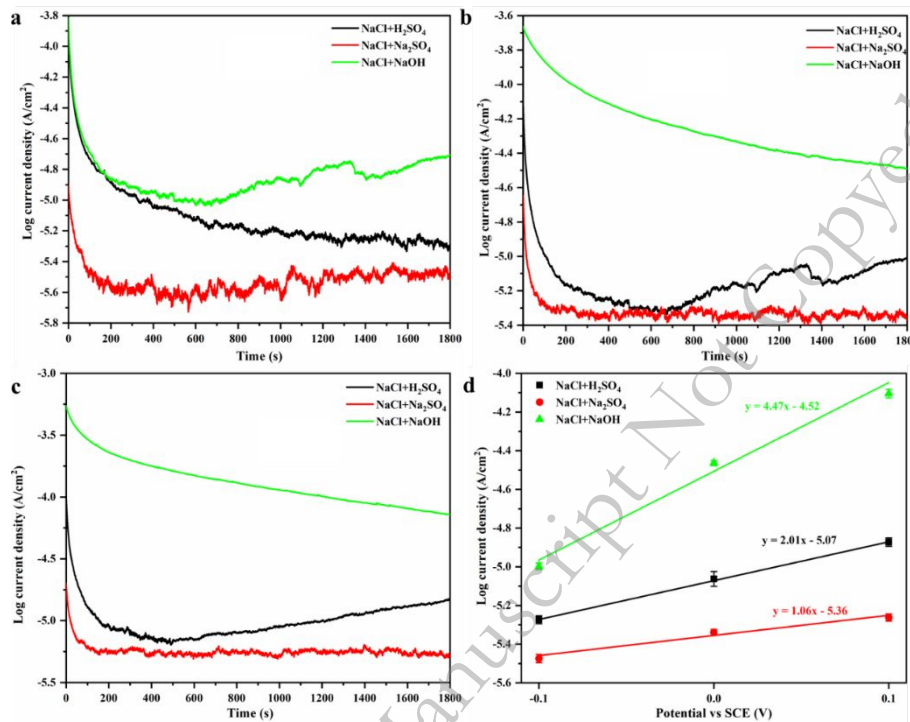
Figure 5 Potentio-static polarisation of LPBF 420 + 5 wt% WC/W_2C MMCs in different solutions at (a) -0.1 V_{SCE}, (b) 0 V_{SCE}, (c) 0.1 V_{SCE}, with (d) average current density at different applied potential and pH solutions.

3.4 Pitting corrosion resistance

Difference corrosion response, from localised corrosion (crevice and pitting corrosion), passivation area, and cathodic reaction area are obtained on the BPE after the bipolar electrochemistry. The pit-covered area on the BPE tested from different solutions between 1 min and 10 min is displayed in Figure 6, the distance between the BPE oxidation and the pits close to the BPE centre is defined by the length covered with pits. For all-optical images, the BPE oxidation edge is positioned on the left side,

where it experiences the highest applied potential. These optical images are captured after immersing the LPBF 420 + 5 wt% WC/W$_2$C MMCs in an ultrasonic bath to eliminate the pit lacy cover. In the presence of H$_2$SO$_4$ + NaCl, no discernible crevice corrosion is observed at the BPE oxidation edge, which exhibits a reduced number of pits, as illustrated in Figure 6 (a1). No visible general corrosion is found on the BPE in an acidic solution, caused by the current density consumed by fast nucleation and propagation of crevice and pitting corrosion, which cannot support the occurrence of pitting corrosion. Figure 6 (b1, c1) displays the optical images of the pit-covered area on the BPE for 5- and 10-minute bipolar exposure. The crevice corrosion next to the BPE oxidation edge becomes visible at 5 min, and the size of the crevice corrosion dramatically increases after 10 min exposure. Pits near BPE oxidation are obtained at 5 min, and then some pits merge with crevice corrosion, which is found after 10 min. Figure 6 (a2, b2, c2) demonstrates the pit-covered length on the BPE tested from Na$_2$SO$_4$ + NaCl; the pits nucleated at high applied potential (next to the BPE oxidation edge) are found after 1 minute of exposure. After 5 minutes, the crevice corrosion is visible, with the largest size and most minor pit numbers detected. The outcomes of the pit-covered length were tested in NaOH + NaCl for 1 min to 10 min, as illustrated in Figure 6 (a3, b3, c3). No large-size crevice corrosion is found in all exposure time, with pit size becoming irregular. The large pits are close to circular without merging with other pits in acidic and neutral solutions. However, the large-size pit on the BPE tested in an alkaline environment is irregular. Also, the large-size pits are not always at the BPE oxidation edge. So, the pit covered length, pit distribution, and pit size were changed by different pH values. SO$_4^{2-}$ and OH$^-$ can retard the nucleation of crevice corrosion in stainless steel, so less crevice corrosion is obtained on the BPE after 1 min exposure [54,55].
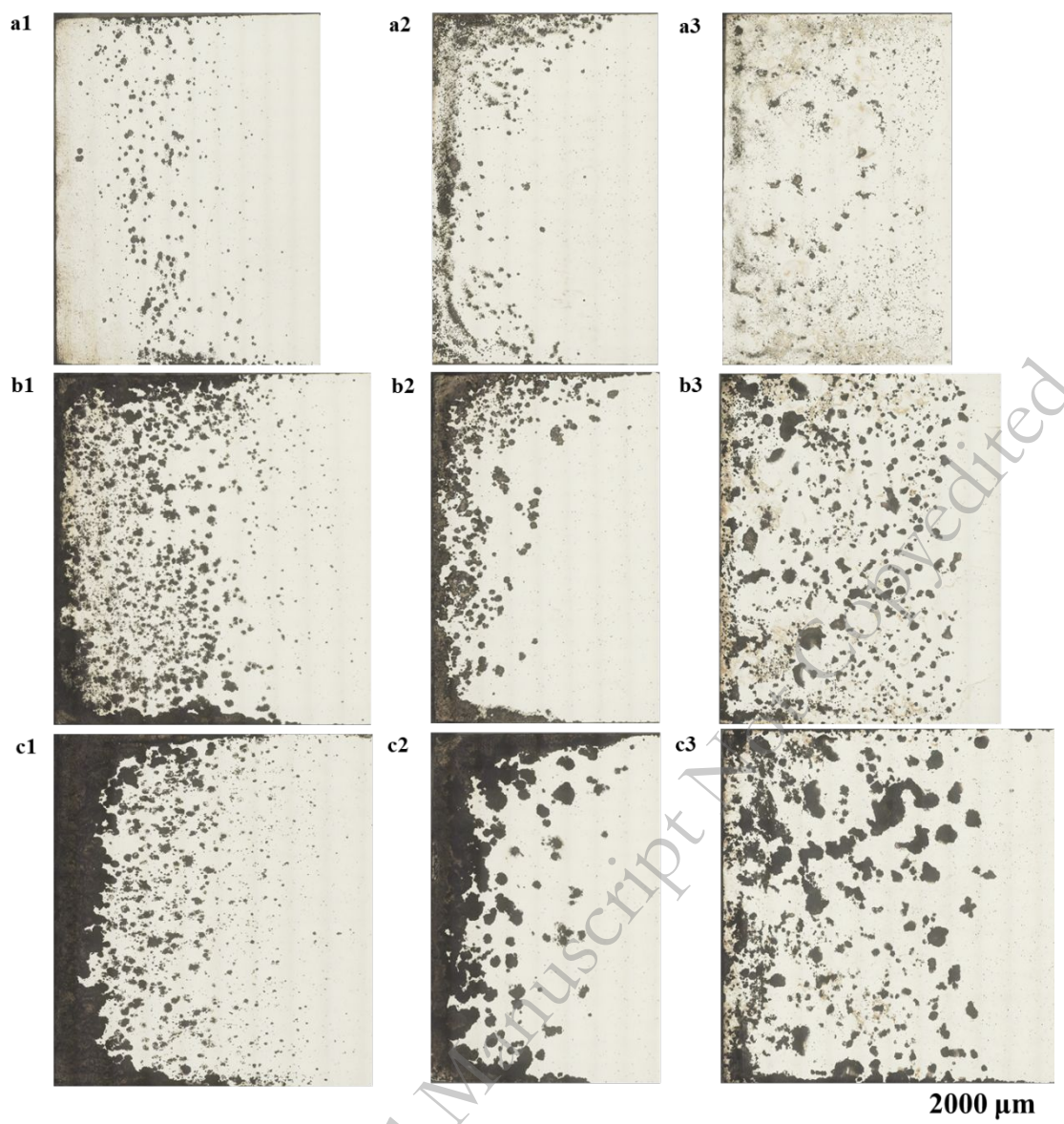
Figure 6 Pit covered length on the BPE tested at (a) 1 min, (b) 5 min, and (c) 10 min. (1: H_2SO_4 + NaCl, 2: Na_2SO_4 + NaCl, 3: NaOH + NaCl).

Figure 7 compares the critical pitting potential (pit-covered length) and localised corrosion growth rate (overall corrosion volume on the BPE) from 1 to 10 min. The bipolar electrochemistry setup is the same in H_2SO_4 + NaCl, Na_2SO_4+ NaCl, and NaOH + NaCl, so there is no difference in the potential distribution of the BPE in different pH solutions. The length values covered by pits signify the critical pitting potential; an increased length of pit coverage correlates with a diminished pitting potential. The total corrosion volume encompasses both pitting and crevice corrosion volumes, with a greater corrosion volume reflecting an accelerated rate of corrosion

progression. Figure 7 (a) compares the pit-covered length on the BPE tested by the different pH value solutions and exposure times. It can be found that the pitting potential reduces after a longer exposure time in acidic, neutral and alkaline solutions, which is related to the cumulative electric charge. Hence, the pit can be nucleated at a lower applied potential region after a longer exposure time [56,57]. The corrosion-covered length is longest in H_2SO_4 + NaCl and shortest in Na_2SO_4 + NaCl. A linear correlation has been established between the length covered by pits and the duration of exposure, with the slope of this relationship for varying exposure times also determined. A steeper slope indicates that the critical pitting potential becomes more readily achievable at a lower applied potential following an extended exposure period. The lowest slope (102.47) is detected in Na_2SO_4 + NaCl, whereas the highest slope is found in NaOH + NaCl (201.43), not H_2SO_4 + NaCl (144.99). The pitting corrosion potential tested from NaOH + NaCl is most sensitive to time, with the critical pitting potential in NaOH + NaCl being lower than H_2SO_4 + NaCl after a relatively long exposure time due to the different slopes. Figure 7 (b) compares the overall corrosion volume on the BPE in various solutions and soaking periods. Interestingly, the lowest corrosion volume is found on the BPE tested in NaOH + NaCl, with the fastest corrosion rate obtained from H_2SO_4 + NaCl, which is opposite to the rank of corrosion performance based on the critical pitting potential. The accelerated increase in corrosion volume from 1 to 5 minutes, compared to the interval between 5 and 10 minutes, may be attributed to intensified competition between pitting and crevice corrosion, which affects the overall corrosion growth rate.
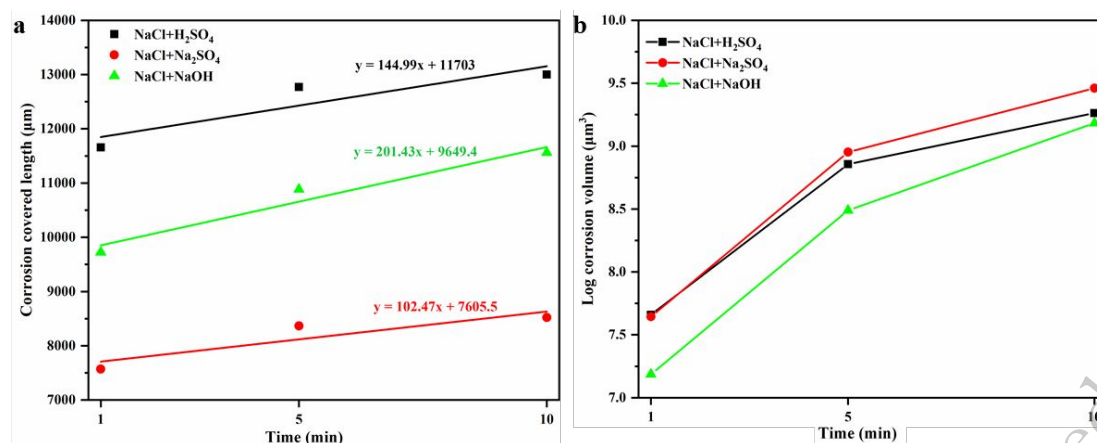
Figure 7 Evolution of (a) pit covered length and (c) corrosion volume loss on BPE in acidic, neutral, and alkaline environments from 1 min to 10 min.

Figure 8 depicts the maximum pit depth alongside the associated pit volume observed in the BPE subjected to H_2SO_4 + NaCl, Na_2SO_4 + NaCl, and NaOH + NaCl over a duration ranging from 1 minute to 10 minutes. Figure 8 (a) illustrates the relationship between pit depth and pit volume on the BPE following a 1-minute exposure, revealing that the deepest pits (reaching up to 35 μm) are predominantly located on the BPE in alkaline conditions; at the same time, the deepest pits tested from acidic and neutral solution are less than 25 μm. However, the pits formed in acidic and neutral solutions have a larger pit volume than those nucleated in an alkaline environment with the same maximum pit depth. Figure 8 (b) and Figure 8 (c) illustrate the correlation of pit depth and volume as assessed from various solutions at the 5-minute and 10-minute marks, respectively. Following the 5-minute interval, the maximum pit depth observed on the BPE across all solutions converges. A linear regression is established between pit depth and volume, with the slope value utilized to interpret the directions of pit growth. Compared to the slight slope, the giant pit slope indicates that large pit volume is increased with the same increase in pit depth, which means pit growth is faster in the pit wall directions. The slope changed by different pH value solutions and exposure period is summarised in Figure 8 (d). The slopes are largest at 1 min exposure, then decreasing with longer exposure time until 10 min, which means its growth in the pit wall directions becomes slower with longer exposure time. The highest slope is obtained in Na_2SO_4 + NaCl, and the lowest is

found in NaOH + NaCl; however, the gaps in different pH solutions are decreasing with longer exposure time.
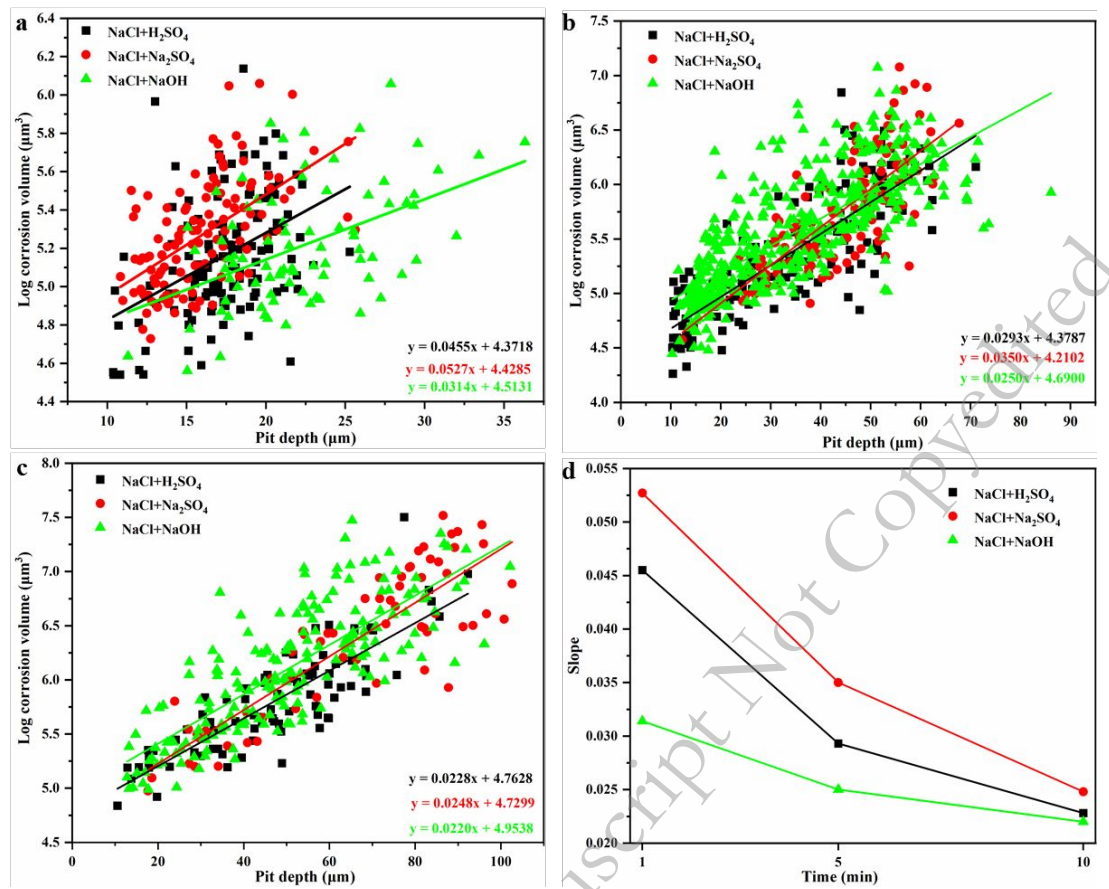

Figure 8 Maximum pit depth and the corresponding pit volume on BPE tested in different solutions at (a) 5 min, (b) 10 min, and (c) 15 min., with (d) changes of pits shapes with different pH environment from 5 min to 15 min.

3.4 Post observation of pitting

The optical and 3D topographical images of the pits observed on the BPE after a 10-minute exposure in H_2SO_4 + NaCl, Na_2SO_4 + NaCl, and NaOH + NaCl are presented in Figure 9. These optical images are obtained without running the ultrasonic bath cleaning, so pit lacy covers are retained on the surface. Figure 9 (a-c) illustrates the optical images of the BPE subjected to testing in an acidic solution. The cast WC/W_2C surface exhibits a darkened appearance following the bipolar electrochemistry experiment, signifying that corrosion has taken place on the reinforced particle, as depicted in Figure 9 (a). Figure 9 (b, c) illustrates that the pits

are initiated adjacent to the reinforced particles, influenced by the galvanic interaction between the cast WC/W_2C and the stainless steel matrix [58,59]. Both the lacy cover (Figure 9 (b)) pit and open pit (Figure 9 (c)) are found next to the strengthened particles obtained on the BPE. Figure 9 (d-f) displays the pit nucleates next to the reinforced particles, in which the surface of the reinforced particles is relatively clean, indicating less corrosion occurs on cast WC/W_2C. Also, the area next to the reinforced particles is the pit nucleation-sensitive site. Interestingly, the concentrated corrosion on the cast WC/W_2C is obtained on the BPE from the $NaOH + NaCl$ solution, in which the surface of the matrix is relatively clean, indicating no/minor corrosion, as shown in Figure 9 (g, h). In Figure 9 (g), part of the reinforced particle has a lower height than the matrix, indicates a fast corrosion rate. The corrosion can remove the reinforced particle altogether, as the whole of the reinforced particle shows a lower height than the matrix, as shown in   Figure 9 (h). So, the area next to the reinforced particles offers the pit nucleation in acidic and neutral solutions, with the cast WC/W_2C preferred to corrode away in the alkaline solutions.
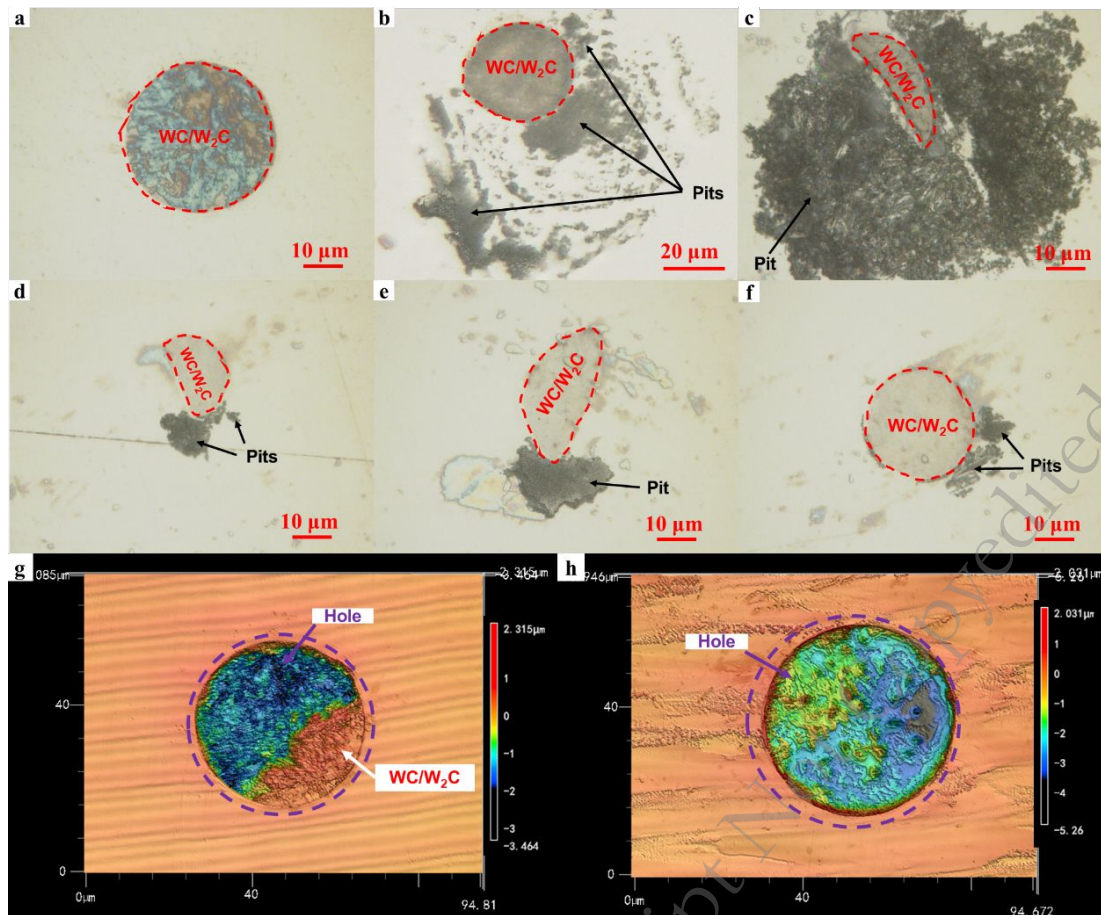
Figure 9 Corrosion response on BPE from (a-c) H_2SO_4 + NaCl, (d-f) Na_2SO_4 + NaCl, and (g, h) NaOH + NaCl.

The pit induction resulting from reinforced particles in the LPBF 420 + 5 wt% WC/W_2C MMCs in a NaOH + NaCl solution is presented in Figure 10. Initially, the corrosion that occurred on the reinforced particles with no corrosion at the matrix, as shown in Figure 10 (a). Figure 10 (b) displays that the reinforced particle stands lower than the matrix, with a feather-like structure on the cast WC/W_2C surface. The feather-like structure is the W_2C, coming from the fast dissolution of the WC from the cast WC/W_2C. In Figure 10 (c) and Figure 10 (d), the side of the hole becomes smooth as the cast WC/W_2C is completely corroded away, and the smooth part should be the stainless-steel matrix. So, corrosion occurred at the reinforced particles nucleate the pitting corrosion; so, the maximum pit depth can quickly reach about 35 μm after 1 min exposure, which should be the largest diameter of reinforced particles in the LPBF MMCs. After that, the holes left from the completely dissolved cast WC/W_2C are the pit electrolyte with a high concentration of Cl$^-$ and low pH value,

which the local aggressive electrolyte and occulted geometry of the encourage the corrosion continue growth as pitting corrosion [60,61]. The dissimilar reinforced particle size and relatively non-uniform distribution of the cast WC/W_2C results in an irregular pit shape on the BPE tested in alkaline solutions. The cross-sectional area of the pit is associated with the distribution of cast WC/W_2C, rather than solely depending on the applied potential. Hence, some pits contain larger areas at a lower applied potential region on the BPE, as locally more numbers and larger size of reinforced particles are more accessible to connect, forming irregular and large pits. From these SEM images, it can be found that feature-like W_2C remains on the cast WC/W_2C, which means the corrosion speed of WC should be faster than W_2C. At the same time, the stainless-steel matrix and *in-situ* reaction layers retained after the reinforced particles are corroded away indicate no/minor corrosion during the bipolar exposure period. Here, the localised corrosion occurs at the reinforced particle on the LPBF 420 + 5 wt% WC/W_2C MMCs, and the propagation of the pits via consuming the cast WC/W_2C until the reinforced particles are entirely removed.
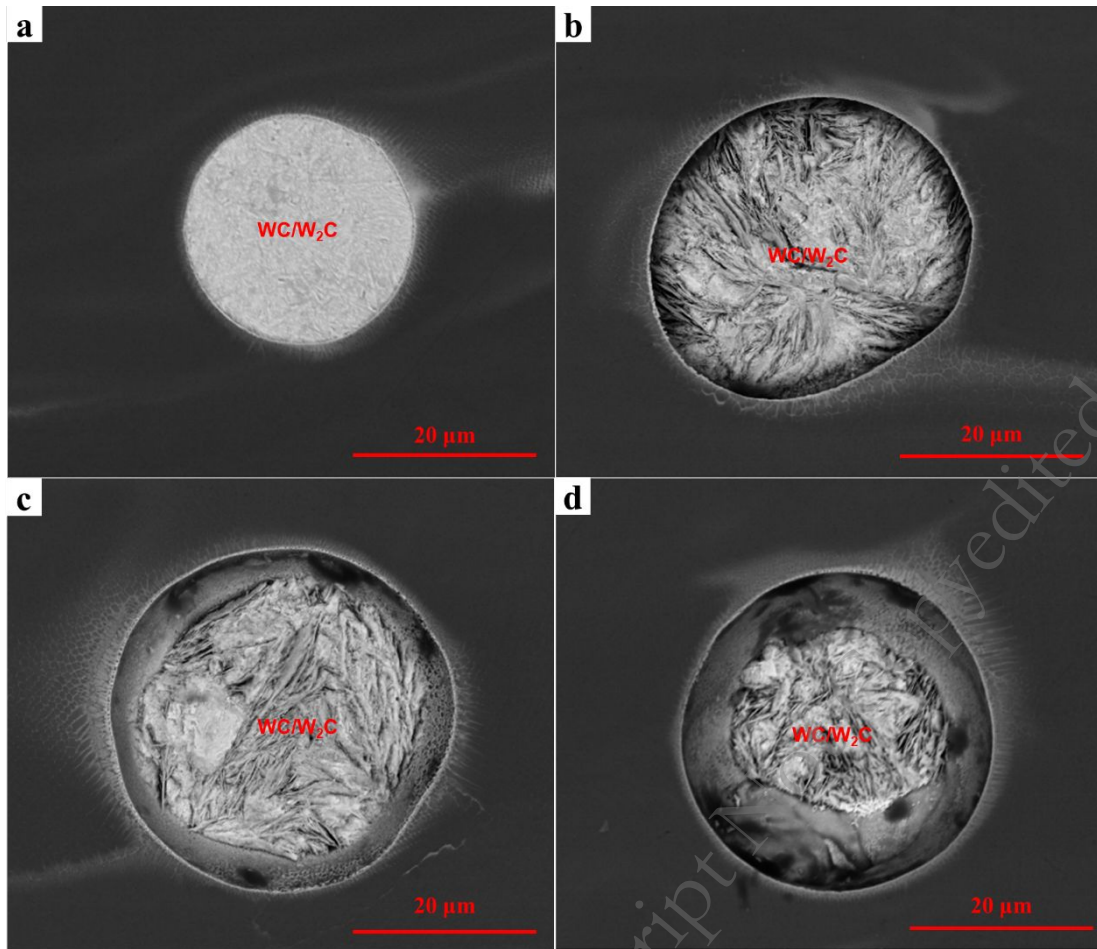
Figure 10 (a-d) Nucleation and growth of localised corrosion on LPBF 420 + 5 wt% WC/W$_2$C MMCs BPE tested in NaOH + NaCl.

The surface of reinforced particles inside pitting corrosion from acidic and neutral solutions is displayed in Figure 11. Figure 11 (a) and Figure 11 (b) show the reinforced particles inside the pits tested in H$_2$SO$_4$ + NaCl and Na$_2$SO$_4$ + NaCl, respectively, with the reinforced particles showing spherical and irregular elliptical shapes. Interestingly, the fur-like *in-situ* reaction layers on the reinforced particles, marked as blue arrows, indicate a higher corrosion resistance than the matrix. Also, a cellular-like structure is found on the reinforced particles, which should be the *in-situ reaction* layers. The size and direction of the cellular structure on the reinforced particles are not the same, coming from the connect to different grain orientation. Figure 11 (c) shows a cast WC/W$_2$C suffering the general corrosion in an acidic solution, in which W$_2$C is not visible, which differs from the corrosion response in the alkaline solutions. Figure 11 (d) shows that the pit bottom consists of cellular

structures with various sizes and directions from different grain orientations. The surface of the cast WC/W$_2$C suffers corrosion in Na$_2$SO$_4$ + NaCl at a very high applied potential region on the BPE, with some cracks, obtained on the surface, as displayed in Figure 11 (e), which is different from the corrosion responses in H$_2$SO$_4$ + NaCl and Na$_2$SO$_4$ + NaCl. The surface outcome of the pit bottom from LPBF 420 + 5 wt% WC/W$_2$C MMCs tested in neutral solution is displayed in Figure 11 (f), with different sizes and directions of the cellular structure seen, which are similar to the pit bottom appearance in acidic solutions.
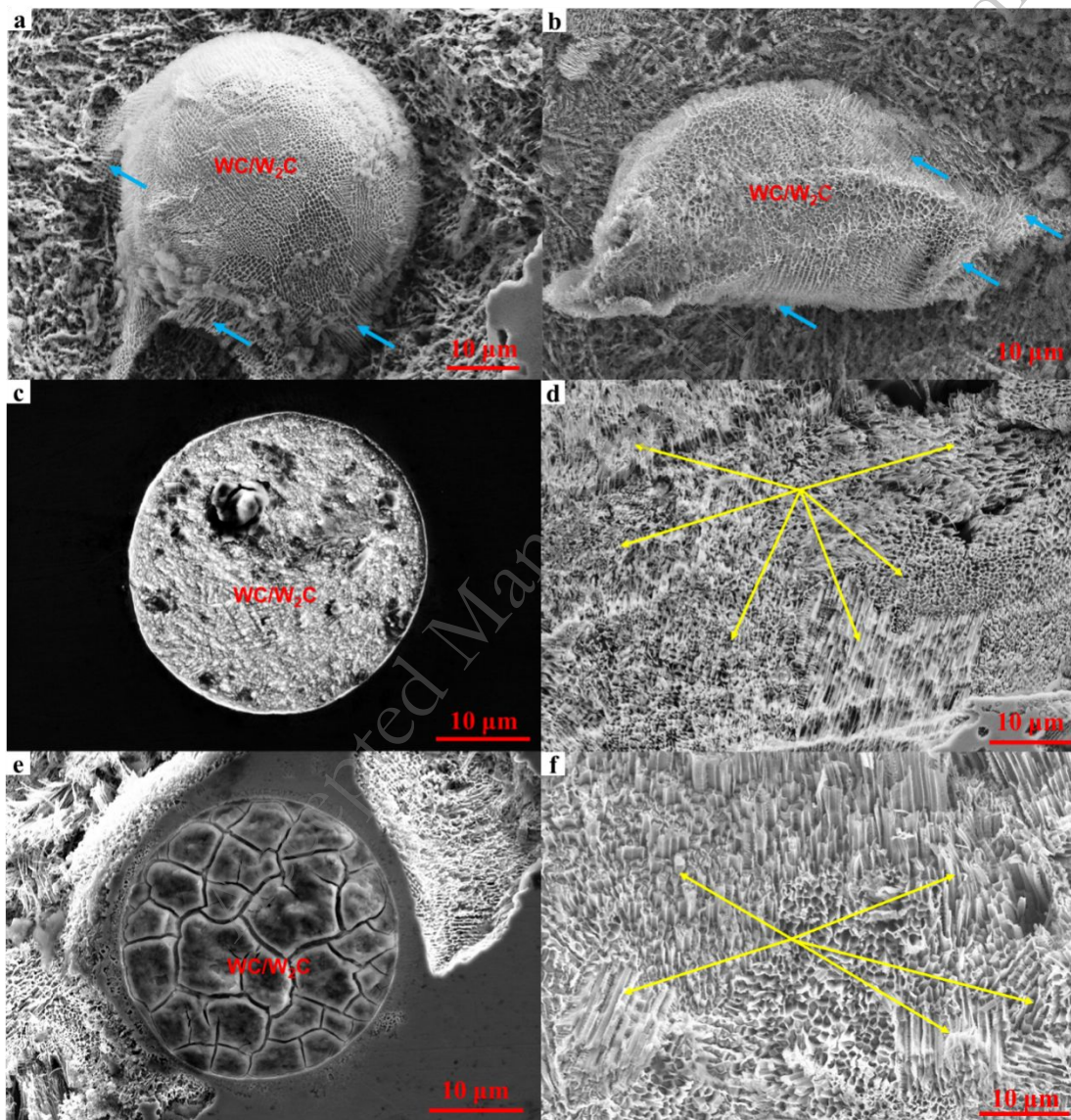

Figure 11 (a,b) reinforced particles tested inside of the pits, (c) appearance of strengthen particle and (d) inside of pits tested in H$_2$SO$_4$ + NaCl, with the corrosion morphologies of spherical cast WC/W$_2$C and pit bottom from Na$_2$SO$_4$ + NaCl. (e, f) corrosion appearance on cast WC/W$_2$C and inside of pit tested in NaOH + NaCl solution.

The *in-situ* reaction layers next to large pits in acidic, neutral, and alkaline solutions are displayed in Figure 12. In Figure 12 (a1), a cast WC/W$_2$C surrounded by a large pit is obtained after exposure to an acidic solution, in which the surface of the reinforced particles suffers general corrosion. A high magnification of *in-situ* reaction layers from the yellow square is shown in Figure 12 (a2), in which the fur-like *in-situ* reaction layer, labelled as blue arrows, with the surrounding matrix corroded away. Figure 12 (b1) demonstrates the pitting corrosion in Na$_2$SO$_4$+ NaCl, which reinforced particle next to the pitting corrosion; and the cast WC/W$_2$C also suffers general corrosion, resulting in a relatively rough surface. Figure 12 (b2) gives the highlighted area from Figure 12 (b1); the results show that *in-situ* reaction layers are retained after the bipolar electrochemistry tests. Figure 12 (c1) and Figure 12 (d1) show two large reinforced particles next to the large-size pits; the large reinforced particle in Figure 12 (c1) is partly dissolved, and the retained cast WC/W$_2$C are seen. The strengthened particles in Figure 12 (c1) is entire, which the smooth surface of the holes from the completely dissolved cast WC/W$_2$C. The higher magnification images of the *in-situ* layer are illustrated in Figure 12 (c2) and Figure 12 (d2), in which the stainless-steel matrix is corroded away as the high applied potential, with the *in-situ* reaction layers retained. The *in-situ* reaction layers maintain a relatively higher corrosion resistance than the stainless steel matrix in an acidic and neutral environment, as the higher W concentration in the reaction layers offers better corrosion resistance than stainless steel [62]. In the alkaline environment, the *in-situ* reaction layer corrodes slower than the reinforced particle, coming from a higher content of Fe. In the acidic and neutral solution, the pits start next to the reinforced particles, related to the Cr-deletion region or galvanic effects. A large number of Cr-rich carbides next to the *in-situ* reaction layers, as shown in Figure 3 (a), in which the large area of the Cr-depletion area is the driving force for pit nucleation [63]. Also, these carbides reduce the stability of the passive film in the stainless steel matrix at a relatively high applied potential; so, the pitting corrosion on the stainless steel is also obtained in the alkaline environment, as displayed in Figure 12 (c, d). Overall, the *in-situ* reaction layers have higher corrosion

resistance than the stainless steel matrix and cast WC/W$_2$C in acidic, neutral, and alkaline solutions.
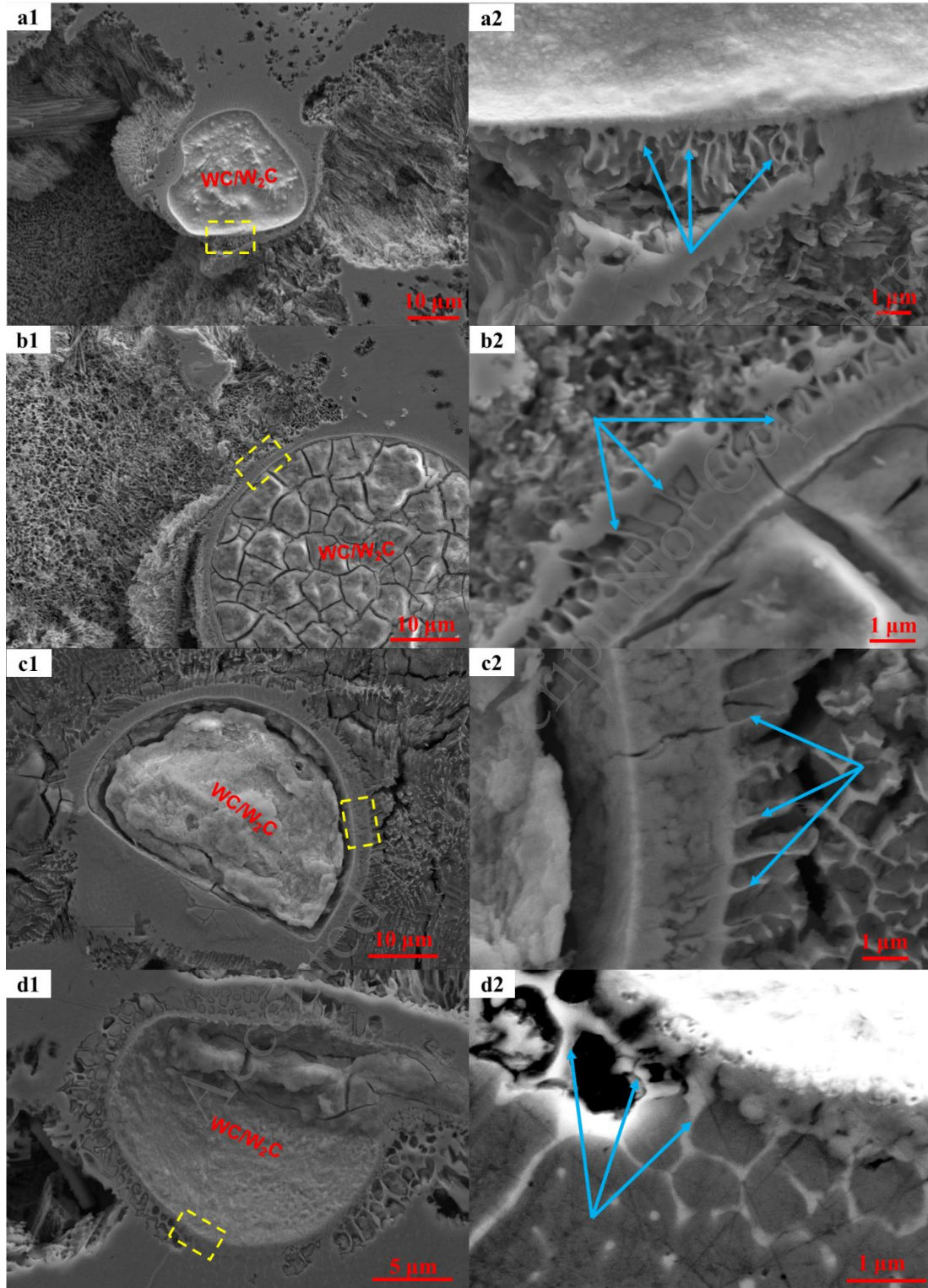

Figure 12 SEM images of stability of *in-situ* reaction layers next to pitting corrosion from (a) H$_2$SO$_4$ + NaCl, (b) Na$_2$SO$_4$ + NaCl, and (c,d) NaOH + NaCl.

4 Conclusions

This paper studies the roles of spherical cast WC/W_2C in pitting corrosion for LPBF 420 + 5 wt% WC/W_2C MMCs in H_2SO_4+ NaCl, Na_2SO_4 + NaCl, and NaOH + NaCl, the main conclusions follow:

1. The dense and crack-free *in-situ* reaction layers are built between the reinforced particle and matrix during the laser scanning. Many Cr-rich precipitates are in the stainless-steel matrix next to the *in-situ* reaction layer.

2. The pit is nucleated next to the cast WC/W_2C, as the galvanic coupling and Cr-depletion region in the acidic and neutral solutions. In contrast, the pit starts from the preferred dissolution of reinforced particles in alkaline solutions. The *in-situ* reaction layers are retained after the pit growth to a relatively large size in all pH value solutions.

3. Adding reinforced particles results in a degradation of passive film and pitting corrosion performance in an alkaline environment. The corrosion rank from the pit nucleation potential is neutral > alkaline > acidic. However, pit growth is fastest in a neutral solution, followed by acidic, and slowest in an alkaline environment.

Data Availability

Data will be made available on request.

CRediT authorship contribution statement

Y. Zhou: Sample preparation, Conceptualization, Methodology, Validation, Formal analysis, Investigation, Data curation, Writing – original draft. L. Li, D. Kong: Formal analysis, Writing – review & editing. P. Hu, S. Wang, T. Liu: Sample preparation. Y. Yan: Validation, Formal analysis, Writing – review & editing. X. Qu, C. Dong, X. Li: Resources, Project administration

References:

[1] L. Raami, T. Varis, K. Valtonen, M. Wendler, O. Volkova, P. Peura, Enhancing the cavitation erosion resistance of AISI 420-type stainless steel with quenching and partitioning, Wear 526–527 (2023). https://doi.org/10.1016/j.wear.2023.204897.

[2] C.J. Scheuer, L.J. Silva, J.C.K. das Neves, R.P. Cardoso, S.F. Brunatto, Tribological performance of low-temperature plasma carburized AISI 420 martensitic stainless steel, Surf Coat Technol 476 (2024). https://doi.org/10.1016/j.surfcoat.2023.130239.

[3] K. Morshed-Behbahani, N. Zakerin, P. Najafisayar, M. Pakshir, A survey on the passivity of tempered AISI 420 martensitic stainless steel, Corros Sci 183 (2021) 109340. https://doi.org/10.1016/j.corsci.2021.109340.

[4] V.B. Vukkum, R.K. Gupta, Review on corrosion performance of laser powder-bed fusion printed 316L stainless steel: Effect of processing parameters, manufacturing defects, post-processing, feedstock, and microstructure, Mater Des 221 (2022). https://doi.org/10.1016/j.matdes.2022.110874.

[5] D. Kong, C. Dong, S. Wei, X. Ni, L. Zhang, R. Li, L. Wang, C. Man, X. Li, About metastable cellular structure in additively manufactured austenitic stainless steels, Addit Manuf 38 (2021) 101804. https://doi.org/10.1016/j.addma.2020.101804.

[6] A. Hemmasian, S. Guo, J. Raush, Corrosion performance of additively manufactured stainless steel parts: A review, Addit Manuf 37 (2021) 101689. https://doi.org/10.1016/j.addma.2020.101689.

[7] D. Kong, C. Dong, X. Ni, L. Zhang, J. Yao, C. Man, X. Cheng, K. Xiao, X. Li, Mechanical properties and corrosion behavior of selective laser melted 316L stainless steel after different heat treatment processes, J Mater Sci Technol 35 (2019) 1499–1507. https://doi.org/10.1016/j.jmst.2019.03.003.

[8] Y. Tian, K. Chadha, C. Aranas, Laser powder bed fusion of ultra-high-strength 420 stainless steel: Microstructure characterization, texture evolution and mechanical properties, Materials Science and Engineering: A 805 (2021).

https://doi.org/10.1016/j.msea.2021.140790.

[9] A. Shahriari, M. Ghaffari, L. Khaksar, A. Nasiri, A. Hadadzadeh, B.S. Amirkhiz, M. Mohammadi, Corrosion resistance of 13wt.% Cr martensitic stainless steels: Additively manufactured CX versus wrought Ni-containing AISI 420, Corros Sci 184 (2021). https://doi.org/10.1016/j.corsci.2021.109362.

[10] A. Moura, L. Favarato, D. Amorim, C. Alcântara, M. Marques, M. Orlando, E. Vieira, W. Labiapari, M. Cunha, T. Oliveira, Effect of austenitization temperature on microstructure, crystallographic aspects, and mechanical properties of AISI 420 martensitic stainless steel, Materials Science and Engineering: A 909 (2024). https://doi.org/10.1016/j.msea.2024.146835.

[11] Y. Zhou, D.L. Engelberg, Accessing the full spectrum of corrosion behaviour of tempered type 420 stainless steel, Materials and Corrosion 72 (2021) 1718–1729. https://doi.org/10.1002/maco.202112442.

[12] A. Vahedi Nemani, M. Ghaffari, S. Salahi, A. Nasiri, Effects of post-printing heat treatment on the microstructure and mechanical properties of a wire arc additive manufactured 420 martensitic stainless steel part, Materials Science and Engineering: A 813 (2021). https://doi.org/10.1016/j.msea.2021.141167.

[13] Y. Fang, Y. Zhang, M.K. Kim, T. Kim, Z. Duan, Q. Yuan, J. Suhr, Multi-scale hybrid reinforced super duplex stainless steel matrix composites with high strength and ductility via laser powder bed fusion and an in-situ synthesis strategy, Addit Manuf 85 (2024). https://doi.org/10.1016/j.addma.2024.104152.

[14] A. Chakraborty, J.K. Singh, D. Sen, S. Pityana, I. Manna, S. Krishna, J. Dutta Majumdar, Microstructures, wear and corrosion resistance of laser composite surfaced austenitic stainless steel (AISI 304 SS) with tungsten carbide, Opt Laser Technol 134 (2021). https://doi.org/10.1016/j.optlastec.2020.106585.

[15] X. Yin, Q. Zhai, Q. Zhang, K. Wang, L. Meng, Z. Ma, G. Chen, S. Wang, L. Wang, Effect of tungsten particles on microstructure and properties of 316 L stainless steel manufactured by selective laser melting, J Manuf Process 68 (2021) 210–221. https://doi.org/10.1016/j.jmapro.2021.05.039.

[16] Y. Zou, C. Tan, Z. Qiu, W. Ma, M. Kuang, D. Zeng, Additively manufactured SiC-reinforced stainless steel with excellent strength and wear resistance, Addit Manuf 41 (2021). https://doi.org/10.1016/j.addma.2021.101971.

[17] Y. Zhou, L. Wang, D. Kong, B. Zhang, T. Liu, Y. Yan, L. Zhang, X. Li, D. Engelberg, C. Dong, Ultra-high strength metal matrix composites (MMCs) with extended ductility manufactured by size-controlled powder and spherical cast tungsten carbide, Compos Part A Appl Sci Manuf 182 (2024) 108194. https://doi.org/10.1016/j.compositesa.2024.108194.

[18] Y. Zhou, Z. Huang, S. Wang, W. Qin, D. Kong, T. Liu, Y. Yan, X. Li, X. Qu, D. Engelberg, C. Dong, Synergistic improvement of pitting and wear resistance of laser powder bed fusion 420 stainless steel reinforced by size-controlled spherical cast tungsten carbides, Corros Sci 237 (2024) 112342. https://doi.org/10.1016/j.corsci.2024.112342.

[19] A. Pardo, E. Otero, M.C. Merino, M.D. López, M. V Utrilla, F. Moreno, Influence of pH and Chloride Concentration on the Pitting and Crevice Corrosion Behavior of High-Alloy Stainless Steels, 2000.

[20] H.S. Klapper, J. Stevens, G. Wiese, Pitting corrosion resistance of CrMn austenitic stainless

steel in simulated drilling conditions - Role of pH, temperature, and chloride concentration, Corrosion 69 (2013) 1095–1102. https://doi.org/10.5006/0947.

[21] L. Li, C.F. Dong, K. Xiao, J.Z. Yao, X.G. Li, Effect of pH on pitting corrosion of stainless steel welds in alkaline salt water, Constr Build Mater 68 (2014) 709–715. https://doi.org/10.1016/j.conbuildmat.2014.06.090.

[22] Y. Zhou, Y. Liu, S. Wang, Z. Yue, Y. Ji, W. Qin, D. Kong, X. Wu, J. Liu, W. Huang, C. Dong, The corrosion performance for ultrafine WC-12Co processed by heat treatments in different pH solution, Int J Refract Metals Hard Mater (2024) 106878. https://doi.org/10.1016/j.ijrmhm.2024.106878.

[23] W. Tang, L. Zhang, Y. Chen, H. Zhang, L. Zhou, Corrosion and strength degradation behaviors of binderless WC material and WC–Co hardmetal in alkaline solution: A comparative investigation, Int J Refract Metals Hard Mater 68 (2017) 1–8. https://doi.org/10.1016/j.ijrmhm.2017.06.003.

[24] L. Liu, M. Yao, Y. Wang, Y. Jin, J. Ji, H. Luo, Y. Cao, Y. Xiong, Y. Sheng, X. Li, D. Qiu, L. Xi, J. Xi, W. Zhang, L. Chen, J. Yang, The MatHub-3d first-principles repository and the applications on thermoelectrics, Materials Genome Engineering Advances (2024). https://doi.org/10.1002/mgea.21.

[25] Y. Zhou, B. Wu, J. Wang, H. Wang, Effect of signal-to-noise ratio on the automatic clustering of X-ray diffraction patterns from combinatorial libraries, Materials Genome Engineering Advances (2024). https://doi.org/10.1002/mgea.27.

[26] Y. Shang, Z. Xiong, K. An, J.A. Hauch, C.J. Brabec, N. Li, Materials genome engineering accelerates the research and development of organic and perovskite photovoltaics, Materials Genome Engineering Advances (2024). https://doi.org/10.1002/mgea.28.

[27] C. Ren, L. Ma, D. Zhang, X. Li, A. Mol, High-throughput experimental techniques for corrosion research: A review, Materials Genome Engineering Advances (2023). https://doi.org/10.1002/mgea.20.

[28] Y. Zhou, S. Mahmood, D.L. Engelberg, High throughput screening of localised and general corrosion in type 2205 duplex stainless steel at ambient temperature, International Journal of Minerals, Metallurgy and Materials (2023). https://doi.org/10.1007/s12613-023-2651-4.

[29] Y. Zhou, N. Stevens, D.L. Engelberg, Corrosion electrochemistry with a segmented array bipolar electrode, Electrochim Acta 375 (2021) 137668. https://doi.org/10.1016/j.electacta.2020.137668.

[30] Y. Zhou, S. Mahmood, D.L. Engelberg, A novel high throughput electrochemistry corrosion test method – bipolar electrochemistry, Curr Opin Electrochem (2023) 101263. https://doi.org/10.1016/j.coelec.2023.101263.

[31] Y. Zhou, S. Mahmood, D.L. Engelberg, Bipolar electrochemistry for high throughput screening of localised corrosion in stainless steel rebars, Constr Build Mater 366 (2023) 130174. https://doi.org/10.1016/j.conbuildmat.2022.130174.

[32] S. Munktell, L. Nyholm, F. Björefors, Towards high throughput corrosion screening using arrays of bipolar electrodes, Journal of Electroanalytical Chemistry 747 (2015) 77–82. https://doi.org/10.1016/j.jelechem.2015.04.008.

[33] Y. Zhou, A. Kablan, D.L. Engelberg, Metallographic screening of duplex stainless steel weld microstructure with a bipolar electrochemistry technique, Mater Charact 169 (2020) 110605. https://doi.org/10.1016/j.matchar.2020.110605.

[34] Y. Zhou, D. Engelberg, Development of a two-dimensional bipolar electrochemistry technique for high throughput corrosion screening, Materials Genome Engineering Advances (2024).

[35] Y. Zhou, D.L. Engelberg, Time-lapse observation of pitting corrosion in ferritic stainless steel under bipolar electrochemistry control, Journal of Electroanalytical Chemistry 899 (2021) 115599. https://doi.org/10.1016/j.jelechem.2021.115599.

[36] S. Munktell, M. Tydén, J. Högström, L. Nyholm, F. Björefors, Bipolar electrochemistry for high-throughput corrosion screening, Electrochem Commun 34 (2013) 274–277. https://doi.org/10.1016/j.elecom.2013.07.011.

[37] Y. Zhou, J. Qi, D.L. Engelberg, On the application of bipolar electrochemistry for simulating galvanic corrosion behaviour of dissimilar stainless steels, Electrochem Commun 126 (2021) 107023. https://doi.org/10.1016/j.elecom.2021.107023.

[38] Y. Zhou, S. Mahmood, D. Lars Engelberg, Application of bipolar electrochemistry to assess the corrosion resistance of solution annealed lean duplex stainless steel, Mater Des (2023) 112145. https://doi.org/10.1016/j.matdes.2023.112145.

[39] Y. Zhou, D.L. Engelberg, Fast testing of ambient temperature pitting corrosion in type 2205 duplex stainless steel by bipolar electrochemistry experiments, Electrochem Commun 117 (2020) 106779. https://doi.org/10.1016/j.elecom.2020.106779.

[40] Y. Zhou, D. Engelberg, On the Application of Bipolar Electrochemistry to Characterise the Localised Corrosion Behaviour of Type 420 Ferritic Stainless Steel, Metals (Basel) 10 (2020) 1–13.

[41] Y. Zhou, D.L. Engelberg, Application of bipolar electrochemistry to assess the ambient temperature corrosion resistance of solution annealed type 2205 duplex stainless steel, Mater Chem Phys 275 (2022) 125183. https://doi.org/10.1016/j.matchemphys.2021.125183.

[42] Y. Zhou, Z. Huang, D. Kong, W. Zhou, Y. Lei, L. Zhang, C. Dong, Applying bipolar electrochemistry to assess the corrosion mechanism of HVOF WC-based coatings with varies binders in different environments, Surf Coat Technol 477 (2024) 130252. https://doi.org/10.1016/j.surfcoat.2023.130252.

[43] Y. Zhou, S. Mahmood, D.L. Engelberg, Brass dezincification with a bipolar electrochemistry technique, Surfaces and Interfaces 22 (2021) 100865. https://doi.org/10.1016/j.surfin.2020.100865.

[44] Q. Xiao, W. lei Sun, K. xin Yang, X. feng Xing, Z. hao Chen, H. nan Zhou, J. Lu, Wear mechanisms and micro-evaluation on WC particles investigation of WC-Fe composite coatings fabricated by laser cladding, Surf Coat Technol 420 (2021). https://doi.org/10.1016/j.surfcoat.2021.127341.

[45] M.P. Ryan, D.E. Williams, R.J. Chater, B.M. Hutton, D.S. McPhail, Why stainless steel corrodes, Nature 415 (2002) 770–774. https://doi.org/10.1038/415770a.

[46] L. Wang, C. fang Dong, C. Man, Y. bo Hu, Q. Yu, X. gang Li, Effect of microstructure on corrosion behavior of high strength martensite steel—A literature review, International Journal of Minerals, Metallurgy and Materials 28 (2021) 754–773. https://doi.org/10.1007/s12613-020-2242-6.

[47] K.H. Anantha, C. Örnek, S. Ejnermark, A. Medvedeva, J. Sjöström, J. Pan, In Situ AFM Study of Localized Corrosion Processes of Tempered AISI 420 Martensitic Stainless Steel:

Effect of Secondary Hardening, J Electrochem Soc 164 (2017) C810–C818. https://doi.org/10.1149/2.1261713jes.

[48] P.Q. Zhang, J.X. Wu, W.Q. Zhang, X.Y. Lu, K. Wan~, A pitting mechanism for passive 304 stainless steel in sulphuric acid media containing chloride ions, Corros Sci 34 (1993) 1343–1354.

[49] C. Liu, F. Mao, J. Wang, B. Li, Combined effect of chloride and sulfate ions on the corrosion behavior of Q355B steel in simulated concrete pore solution, Mater Today Commun 40 (2024). https://doi.org/10.1016/j.mtcomm.2024.109703.

[50] L. Zhang, Y. Chen, Q.L. Wan, T. Liu, J.F. Zhu, W. Tian, Electrochemical corrosion behaviors of straight WC-Co alloys: Exclusive variation in grain sizes and aggressive media, Int J Refract Metals Hard Mater 57 (2016) 70–77. https://doi.org/10.1016/j.ijrmhm.2016.02.009.

[51] H. Luo, H. Su, C. Dong, K. Xiao, X. Li, Electrochemical and passivation behavior investigation of ferritic stainless steel in alkaline environment, Constr Build Mater 96 (2015) 502–507. https://doi.org/10.1016/j.conbuildmat.2015.08.052.

[52] L. Freire, M.J. Carmezim, M.G.S. Ferreira, M.F. Montemor, The electrochemical behaviour of stainless steel AISI 304 in alkaline solutions with different pH in the presence of chlorides, Electrochim Acta 56 (2011) 5280–5289. https://doi.org/10.1016/j.electacta.2011.02.094.

[53] K. Bin Tayyab, A. Farooq, A.A. Alvi, A.B. Nadeem, K.M. Deen, Corrosion behavior of cold-rolled and post heat-treated 316L stainless steel in 0.9wt% NaCl solution, International Journal of Minerals, Metallurgy and Materials 28 (2021) 440–449. https://doi.org/10.1007/s12613-020-2054-8.

[54] A.A. Dastgerdi, A. Brenna, M. Ormellese, M.P. Pedeferri, F. Bolzoni, Experimental design to study the influence of temperature, pH, and chloride concentration on the pitting and crevice corrosion of UNS S30403 stainless steel, Corros Sci 159 (2019). https://doi.org/10.1016/j.corsci.2019.108160.

[55] K. Matsumura, M. Nishimoto, I. Muto, Y. Sugawara, Sudden pH and Cl − Concentration Changes during the Crevice Corrosion of Type 430 Stainless Steel , J Electrochem Soc 169 (2022) 101506. https://doi.org/10.1149/1945-7111/ac9bda.

[56] X.L. Zhang, Z.H. Jiang, Z.P. Yao, Y. Song, Z.D. Wu, Effects of scan rate on the potentiodynamic polarization curve obtained to determine the Tafel slopes and corrosion current density, Corros Sci 51 (2009) 581–587. https://doi.org/10.1016/j.corsci.2008.12.005.

[57] P. Ernst, R.C. Newman, Pit growth studies in stainless steel foils. I. Introduction and pit growth kinetics, Corros Sci 44 (2002) 927–941. https://doi.org/10.1016/S0010-938X(01)00133-0.

[58] Y. Chen, B. Yang, Y. Zhou, Y. Wu, H. Zhu, Evaluation of pitting corrosion in duplex stainless steel Fe20Cr9Ni for nuclear power application, Acta Mater 197 (2020) 172–183. https://doi.org/10.1016/j.actamat.2020.07.046.

[59] Z. Ye, L. Guan, Y. Li, J. Zhong, L. Liao, D. Xia, J. Huang, Understanding the galvanic corrosion of Cu-Ni alloy/2205 DSS couple using electrochemical noise and microelectrochemical studies, Corros Sci 224 (2023). https://doi.org/10.1016/j.corsci.2023.111512.

[60] N. Laycock, R. Newman, Localised dissolution kinetics, salt films and pitting potentials, Corros Sci 39 (1997) 1771–1790. https://doi.org/10.1016/S0010-938X(97)00049-8.

[61] P. Ernst, N. Laycock, M. Moayed, R. Newman, The mechanism of lacy cover formation in pitting, Corros Sci 39 (1997) 1133–1136.

[62] T. Lai, P. Sun, H. Sun, W. Song, C. Tang, H. Zhang, M. Chen, D. Wang, Enhancing corrosion resistance and mechanical properties of laser-direct energy deposited 316 stainless steel via W addition, Corros Sci 231 (2024). https://doi.org/10.1016/j.corsci.2024.111960.

[63] Y. Zhao, W. Liu, T. Zhang, Z. Sun, Y. Wang, Y. Fan, B. Dong, Assessment of the correlation between M23C6 precipitates and pitting corrosion resistance of 0Cr13 martensitic stainless steel, Corros Sci 189 (2021). https://doi.org/10.1016/j.corsci.2021.109580.